

Time-resolved observation of thermalization in an isolated quantum system

Govinda Clos,^{1,*} Diego Porras,² Ulrich Warring,¹ and Tobias Schaetz¹

¹*Physikalisches Institut, Albert-Ludwigs-Universität,
Hermann-Herder-Straße 3, 79104 Freiburg, Germany.*

²*Department of Physics and Astronomy, University of Sussex, Brighton BN1 9QH, United Kingdom.*

(Dated: May 8, 2022)

How does statistical mechanics emerge in an isolated quantum system? Part of this question is addressed by a conjecture called Eigenstate Thermalization Hypothesis (ETH), while the debate on the underlying dynamics remains unsettled. We scale a trapped-ion system to study a spin evolving in a Hilbert space of dimension up to 2^{22} by tuning its coupling to a discrete bosonic environment. Controlling external parameters, we increase the effective size of the system and experimentally test ETH predictions: Time averages of local spin observables come to agreement with microcanonical averages while corresponding fluctuations decay. We exploit that our approach features coherent control of all degrees of freedom of an isolated quantum system to study equilibration, thermalization and its dynamics on transient up to effectively infinite time scales.

The relationship between deterministic quantum dynamics and probabilistic classical mechanics has been studied since the early days of quantum mechanics [1]. Consider a quantum system that we initialize out of equilibrium and isolate from any external bath. Can we expect it to feature characteristics of equilibration or even thermalization? How does classical statistical mechanics emerge when size and complexity increase? There is strong evidence that aspects of thermalization can be understood at the level of single quantum states: the ETH predicts that each individual eigenstate of a nonintegrable Hamiltonian [2] yields expectation values of observables identical to microcanonical averages [3–5]. This conjecture is extensively studied by numerical simulations of specific quantum many-body systems of moderate size, exploiting the available computational power [6–9]. Further, progress in the theory of thermalization properties and fluctuations of local observables has been made [10–16]. However, fundamental questions concerning nonequilibrium dynamics of thermalization and relevant time scales remain open [16–18]. Recently, related issues, such as relaxation and prethermalization have been addressed in experiments with ultracold atoms [19–21], opening an exciting perspective to access these phenomena.

Trapped-ion systems are well-suited to study quantum dynamics at a fundamental level, featuring unique control in preparation, manipulation, and detection of electronic and motional degrees of freedom [22]. Their Coulomb interaction of long range permits tuning from weak to strong coupling. Additionally, the system can be scaled bottom-up to the mesoscopic size of interest to investigate many-body physics, beyond one-dimensional systems tractable by approximations [23–25]. In this work, we vary the coupling of a single spin to a bosonic environment continuously scaled in complexity. We tune our trapped-ion system from an integrable to a nonintegrable regime and record its coherent evolution to derive time averages and the scaling of fluctuations with the size of the system. Thereby, we observe the dynamics of ther-

malization and the emergence of statistical mechanics in an isolated mesoscopic quantum system, extending beyond tractability by numerical means.

The dynamics of our system is governed by the Hamiltonian [26, 27]

$$H = \frac{\hbar\Omega_R}{2}\sigma_x + \frac{\hbar\omega_z}{2}\sigma_z + \sum_{m=1}^N \hbar\omega_m a_m^\dagger a_m + \frac{\hbar\Omega_R}{2}(\sigma^+ C + \sigma^- C^\dagger), \quad (1)$$

where a_m (a_m^\dagger) denotes the annihilation (creation) operator of phonons in the m th mode with frequency ω_m , while N is the total number of modes. The spin is described by the Pauli operators σ_l ($l = x, y, z$). We lift the degeneracy of $|\downarrow\rangle$ and $|\uparrow\rangle$, the eigenstates of σ_z , by a transverse field $B_z = \hbar\omega_z$, and couple these states with Rabi frequency Ω_R . The last term in Eq. 1 describes the nonlinear spin-phonon coupling via spin-flips (σ^\pm) with

$$C = \exp\left(i \sum_{m=1}^N \eta_m (a_m^\dagger + a_m)\right) - 1, \quad (2)$$

at a strength tunable by Ω_R and the Lamb-Dicke parameters $\eta_m \sim 1/\sqrt{\omega_m}$. Values $\eta_{m=1\dots N} \ll 1$ lead to linear (weak) coupling, whereas for $\eta_{m=1\dots N} \approx 1$, higher order phonon processes become relevant (strong coupling), allowing the system to explore the full many-body set of highly entangled spin-phonon states. This regime is well described by Exact Diagonalization only, since the discrete nature of the bosonic environment of finite size hinders the application of standard approximations applicable to the spin-boson model considering a continuous spectral density [27, 28]. The natural time scale for dynamics is given by $\tau_R \equiv 1/\Omega_R$, and we denote the duration for which we observe the dynamics by τ_{obs} .

To study nonequilibrium dynamics of expectation values $\langle\sigma_l(t)\rangle$ ($l = x, y, z$), consider an initial product state $\rho(t=0) \equiv \rho(0) = \rho_S(0) \otimes \rho_B(0)$, where the spin is in a

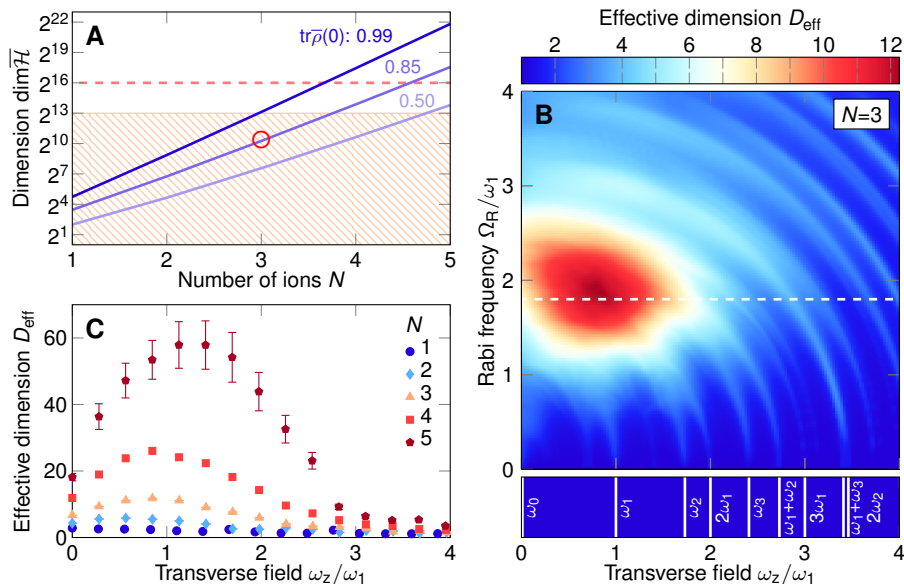


FIG. 1. Complexity of our Hamiltonian studied numerically and computational limitations. Parameters: $\bar{n}_{m=1\dots N} = 1$ and $\eta_1 = 0.54$. (A) Dimension of the truncated Hilbert space $\dim \overline{\mathcal{H}}(N)$ (cf. Eq. 3) for corresponding fractions of initial-state population $\text{tr} \overline{\rho}(0)$ lying within $\overline{\mathcal{H}}$ (solid lines). For $N = 3$, as an example, 85% of the population lie within a space with $\dim \overline{\mathcal{H}} \approx 2^{10}$ (circle), whereas $\dim \overline{\mathcal{H}} \approx 2^{22}$ is required to take into account 99% for $N = 5$. We use $\dim \overline{\mathcal{H}} \leq 2^{13}$ to sample the time evolution $\langle \sigma_z(t) \rangle$ from 0 to τ_{obs} by Exact Diagonalization (shaded area). With numerical approximations we derive $D_{\text{eff}}(N, \Omega_R, \omega_z)$ up to $\dim \overline{\mathcal{H}} = 2^{16}$ (dashed line) [27]. (B) illustrates tunability of $D_{\text{eff}}(\Omega_R, \omega_z)$, here for $N = 3$. At $\{\Omega_R, \omega_z\} \approx \{2, 1\} \times \omega_1$, the spin couples maximally to the modes (sketched at the bottom). The dashed line includes the regime of large D_{eff} , which we study by choosing Ω_R and varying ω_z . (C) We can scale the system with external parameters, here, we show $D_{\text{eff}}(\omega_z)$ for $N = 1 \dots 5$. This enables the investigation of equilibration and thermalization properties depending on the size of the system.

pure excited state, and the bosonic modes are in thermal states close to their ground states ($\bar{n}_{m=1\dots N} \lesssim 1$). We ensure that energies of spin and phonons remain comparable to enable the observation of the coherent quantum nature of the dynamics.

When thermalization occurs, any small subsystem of a large isolated system equilibrates towards a thermal state and remains close to it for most times [10, 13]. The ETH relies on the assumption that a coupling distributes any of the energy eigenstates of an uncoupled system $\{|\phi_\alpha\rangle\}$ over a large subset of the eigenstates of the coupled system $\{|\psi_\beta\rangle\}$, i.e., $|\phi_\alpha\rangle = \sum_\beta c_\beta(\alpha)|\psi_\beta\rangle$ such that the $|\psi_\beta\rangle$ lie within a narrow energy shell around the energy of $|\phi_\alpha\rangle$ [27]. Then, expectation values of observables in the state $|\phi_\alpha\rangle$ give the same result as microcanonical averages. Furthermore, quantifying the dimension D of that subset, the ETH predicts that amplitudes of fluctuations, caused by quantum uncertainties in the (essentially static) state $|\phi_\alpha\rangle$, decay with $1/\sqrt{D}$ [3, 8, 13, 15]. Here, we extend the definition of D for pure states [10, 13] to mixed states $\rho(0) = \sum_\alpha w_\alpha |\phi_\alpha\rangle\langle\phi_\alpha|$ using an effective dimension [27]

$$D_{\text{eff}} \equiv \sum_\alpha w_\alpha \left(\sum_\beta |c_\beta(\alpha)|^4 \right)^{-1}. \quad (3)$$

This renormalizes to the contribution of each single pure state $|\phi_\alpha\rangle$ contained in the mixture. Hence, D_{eff} can be understood as a quantifier of complexity of the quantum dynamics of $\rho(0)$ under the Hamiltonian, and it yields $D_{\text{eff}} = 1$ for the uncoupled system in contrast to other definitions [10, 13, 15]. Following the ETH, infinite-time averages of expectation values

$$\mu_\infty(\sigma_l) \equiv \lim_{\tau \rightarrow \infty} \frac{1}{\tau} \int_0^\tau \langle \sigma_l(t) \rangle dt \quad (4)$$

become equivalent to microcanonical averages $\mu_{\text{micro}}(\sigma_l)$, which approach thermal averages as the system grows in size. Further, we identify the amplitude of fluctuations by the standard deviation

$$\delta_\infty(\sigma_l) \equiv \sqrt{\mu_\infty(\sigma_l^2) - \mu_\infty(\sigma_l)^2}. \quad (5)$$

We approximate $D_{\text{eff}}(N, \Omega_R, \omega_z; \eta_1, \bar{n}_{m=1\dots N})$ (Eq. 3) numerically by truncating the Hilbert space \mathcal{H} to $\overline{\mathcal{H}}$, choosing a phonon number cutoff n_c such that $\dim \overline{\mathcal{H}} = 2(n_c + 1)^N \lesssim 2^{16}$ [27]. For constant computational power and increasing N the truncated initial-state population $\text{tr} \overline{\rho}(0)$ decreases and becomes less representative, leading to increasing systematic uncertainties, illustrated in Fig. 1A. Figure 1B highlights the tunability of D_{eff} , e.g., by applying the transverse field ω_z , while its overall range can be extended by increasing N as presented in Fig. 1C.

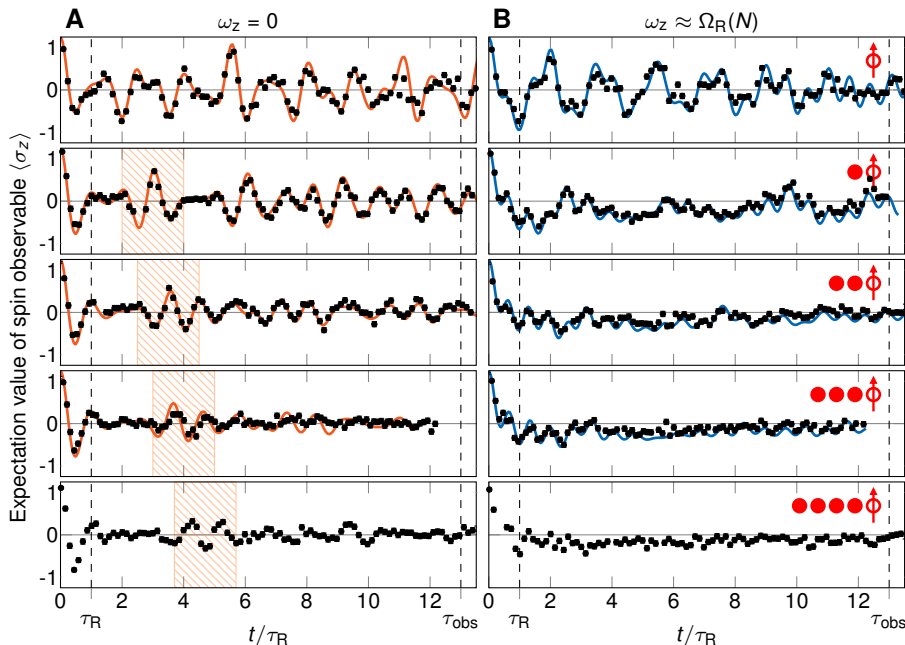


FIG. 2. Unitary time evolution of the spin observable $\langle \sigma_z(t) \rangle$. Experimental results (black dots) with statistical uncertainties (averaging 500 repetitions) and Exact Diagonalizations of the unitary evolution (solid lines) are compared. Red symbols represent the number of ions $N = 1 \dots 5$. We omit numerics for $N = 5$ due to large systematic uncertainties ($\text{tr}\bar{\rho}(0) < 0.5$), see Fig. 1A [27]. The high-amplitude oscillations during the transient duration $t/\tau_R \lesssim 1$ (τ_R and τ_{obs} indicated by dashed lines) are driven by the evolution of $\rho(0)$ towards the ground state of H . (A) For $\omega_z = 0$ and $N = 1$, these oscillations persist, governed by the coupling to the single mode at ω_1 . For $N > 1$, excitation is coherently exchanged with an increasing number of modes resulting in revivals at τ_{rev} (shaded areas). (B) For $\omega_z \approx \Omega_R$ and $N = 1$, oscillations are still driven by the strong coupling to ω_1 , while for $N > 1$, oscillation amplitudes appear damped and $\langle \sigma_z(t) \rangle$ fluctuates around a negative offset ($\mu_{\text{exp}}(\sigma_z) < 0$); this nontrivial bias is a consequence of the applied transverse field and emphasizes the coherence of the dynamics.

We experimentally implement the single pseudo-spin by two electronic hyperfine ground states of $^{25}\text{Mg}^+$ and add up to four $^{26}\text{Mg}^+$ to engineer the size of the bosonic environment spanned by the axial motional modes [27, 29, 30]. First, we prepare the spin state $\rho_S(0) = |\downarrow\rangle\langle\downarrow|$ by optical pumping and initialize the phonon state $\rho_B(0)$ by resolved sideband cooling close to the ground state. We determine in calibration measurements that the modes are in thermal states with $\bar{n}_{m=1\dots N} \lesssim 1$, which effectively enhances $\eta_{m=1\dots N}$ [27]. Next, we apply the spin-phonon interaction by continuously driving two-photon stimulated Raman transitions with Ω_R for variable duration t [26]. We set the strength of the transverse field by detuning from the resonant transition by ω_z . Finally, we detect the spin by state-dependent fluorescence and extract $\langle \sigma_z(t) \rangle$. To explore the regime of large D_{eff} , we choose 95 parameters settings: For $\eta_1 \approx 0.54$, $N = 1 \dots 5$, and $\Omega_R(N) \approx 2\pi \times \{0.7, 1.0, 1.3, 1.4, 1.6\}$ MHz, we vary ω_z from 0 to $2\pi \times 2.8$ MHz.

In Figure 2, we present two example sets of $\langle \sigma_z(t) \rangle$ for $N = 1 \dots 5$ and compare experimental results with those of numerical Exact Diagonalizations of Eq. 1 [27]. The numerical approach for $N = 5$ is severely limited cutting of $> 50\%$ initial-state population, see Fig. 1A. For $\omega_z = 0$ and $N = 1$, we confirm oscillations of high and persist-

ing amplitude due to the coupling to the only mode at ω_1 . For increasing N , the spin couples to N modes including higher order processes, such that spin excitation gets distributed into the growing bosonic environment. Hence, coherent oscillations at incommensurate frequencies lose their common contrast and appear damped. After the transient duration $t/\tau_R \approx 1$, the spin observable remains close to its experimental time average

$$\mu_{\text{exp}}(\sigma_z) \equiv \frac{1}{S_{\text{exp}}} \sum_{t \in [\tau_R, \tau_{\text{obs}}]} \langle \sigma_z(t) \rangle \quad (6)$$

over S_{exp} measured data points within the interval $[\tau_R, \tau_{\text{obs}}]$. Revivals of spin excitation due to the finite size of the system appear at $\tau_{\text{rev}} \sim 1/\delta\bar{E}$, where $\delta\bar{E}$ is the mean energy difference between modes. The coherence of the evolution for large D_{eff} is most evident for $\omega_z \approx \Omega_R$: negative $\mu_{\text{exp}}(\sigma_z)$ indicate equilibration of the spin from $|\downarrow\rangle$ to the ground state of the coupled Hamiltonian (Eq. 1), biased by ω_z . Since our system is near-perfectly isolated within τ_{obs} , our experimental results are well described by unitary time evolution [27].

We summarize our experimental and numerical results in Fig. 3, by deriving time averages $\mu_{\text{exp}}(\sigma_z)$ and corresponding standard deviations, denoted by $\delta_{\text{exp}}(\sigma_z)$, in dependence of ω_z and N and compare these to ETH predic-

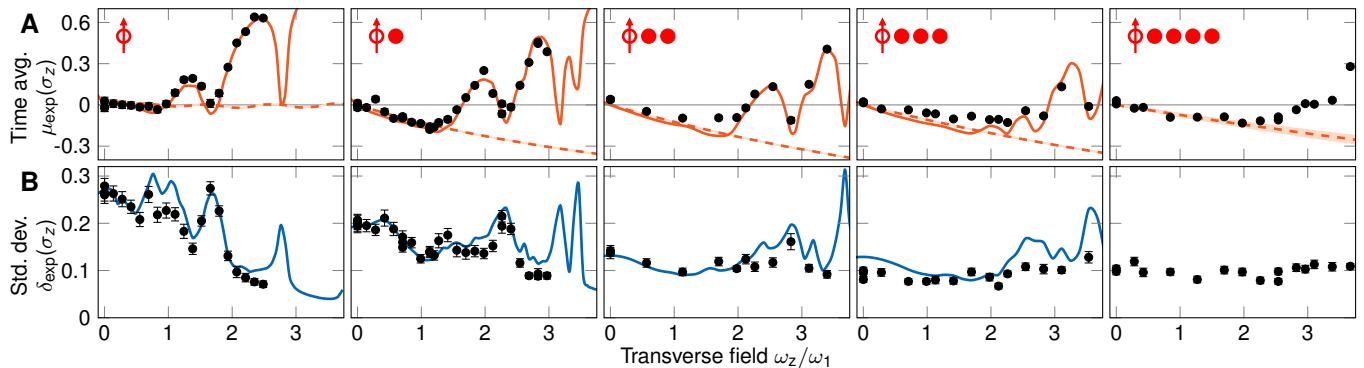


FIG. 3. Comparison of time averages and standard deviations of the time evolution with ETH predictions. Based on experimental traces (cf. Fig. 2), we derive $\mu_{\text{exp}}(\sigma_z)$ and $\delta_{\text{exp}}(\sigma_z)$ (black dots) and compare to Exact Diagonalizations (solid lines) for varying ω_z and $N = 1 \dots 5$. As in Fig. 2, error bars indicate statistical uncertainties and numerics for $N = 5$ are omitted as $\text{tr}\bar{\rho}(0) < 0.5$ [27]. (A) For increasing N , time averages follow microcanonical averages $\mu_{\text{micro}}(\sigma_z)$ (dashed lines) for a wider range of ω_z . The shaded areas indicate systematic uncertainties of $\mu_{\text{micro}}(\sigma_z)$. In (B), $\delta_{\text{exp}}(\sigma_z)$ gradually decreases with N . We find correlated resonances in $\mu_{\text{exp}}(\sigma_z)$ and $\delta_{\text{exp}}(\sigma_z)$ fading away as a function of N indicating that our system is tuned from microscopic to mesoscopic size.

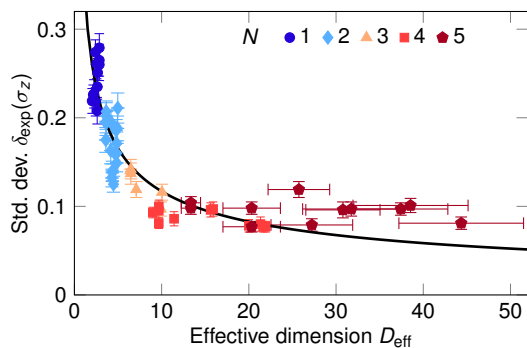


FIG. 4. Scaling of fluctuations with effective system dimension. For each experimental parameter setting, we numerically calculate D_{eff} , attribute systematic uncertainties [27], and plot $\delta_{\text{exp}}(\sigma_z)$ as a function of D_{eff} for $N = 1 \dots 5$. We compare fluctuation amplitudes to the scaling $\sim 1/\sqrt{D_{\text{eff}}}$ (solid line), which is predicted for infinite time and initial pure states. Nevertheless, our measurements for finite duration agree with this scaling for $D_{\text{eff}} \lesssim 25$. Further increasing D_{eff} , the system needs longer durations to resolve the decreasing energy differences δE in the environment, $t \sim 1/\delta E$, unveiling the importance of time scales which requires a description beyond ETH.

tions. We find that $\mu_{\text{exp}}(\sigma_z)$ remains close to $\mu_{\text{micro}}(\sigma_z)$, calculated by Exact Diagonalization, for a larger range of ω_z when increasing N . Finite-size effects of the environment are prominent in resonances of $\mu_{\text{exp}}(\sigma_z)$ and $\delta_{\text{exp}}(\sigma_z)$ for $N = 1$, while their amplitudes gradually fade away for higher N . To study correlations between effective dimension and the amplitude of fluctuations, we combine our experimental results $\delta_{\text{exp}}(\sigma_z)$ with numerical predictions of D_{eff} within ETH. To this end, we select data points well described by microcanonical averages, see Fig. 3A [27]. We plot these in Fig. 4, and find that

$\delta_{\text{exp}}(\sigma_z)$ decreases as a function of D_{eff} (and N), while the ranges of $D_{\text{eff}}(N)$ grow and overlap. The solid line illustrates the scaling with $1/\sqrt{D_{\text{eff}}}$ which is predicted by the ETH for pure initial states and infinite times. Despite our initial mixed state and finite observation duration, our measurements for $D_{\text{eff}} \lesssim 25$ feature this scaling. For larger D_{eff} , the fluctuations do not seem to decrease further, which we attribute to the spin requiring an extended duration to couple to the full bosonic environment. This duration is related to relevant energy differences δE in the environment, $t \sim 1/\delta E$, while the energy density grows exponentially with the size of the system. Our observations emphasize the significance of time scales, providing insight into the dynamics towards thermal equilibrium.

We scale our trapped-ion system including its engineered environment, and reach relevant Hilbert space dimensions of up to 2^{22} , out of reach for state-of-the-art Exact Diagonalization [8]. Exemplarily, we measure time averages and fluctuations of one representative local spin observable and exploit an effective dimension to study their dependence on system size. Comparing to ETH, we observe the emergence of quantum statistical mechanics within our isolated and finite-sized system. Simultaneously, we monitor the coherent dynamics of thermalization, revealing initial and transient behavior, and the evolution towards thermal equilibrium. Thereby, we contribute to open questions in the field of thermalization [16, 31]. Our approach admits to almost arbitrarily generate initial conditions, choosing different spin and phonon states (even nonthermal baths), and preparing initial correlations [22]. In addition, it allows to measure a variety of local spin and phonon observables. Applying those techniques, we can study, e.g., the non-Markovianity of the dynamics, which is evidenced by re-

vivals in the evolution, in detail [32]. Further, increasing the strength of the spin-phonon coupling, we can effectively extend the observed time span. Possible extensions include incorporating more and larger spins, tuning long-range interactions, and adding external baths [26, 33, 34], to propel experimental quantum simulations.

During completion of our manuscript, we got aware of related work on many-body localization inhibiting thermalization in a system of trapped ions [35].

We thank H.-P. Breuer for useful discussions and M. Enderlein, J. Pacer, and J. Harlos for assistance during the setup of the experiment. This work was supported by the Deutsche Forschungsgemeinschaft (SCHA 973), the People Programme (Marie Curie Actions) of the European Union's Seventh Framework Programme (FP7/2007-2013, REA grant agreement no: PCIG14-GA-2013-630955) (D.P.), and the Freiburg Institute for Advanced Studies (FRIAS) (T.S.).

in Physics **75**, 024401 (2012).

- [24] C. Monroe, J. Kim, *Science* **339**, 1164 (2013).
- [25] M. Ramm, T. Pruttivarasin, H. Häffner, *New Journal of Physics* **16**, 063062 (2014).
- [26] D. Porras, F. Marquardt, J. von Delft, J. I. Cirac, *Physical Review A* **78**, 010101 (2008).
- [27] For further details, see Supplementary Material.
- [28] A. J. Leggett, *et al.*, *Reviews of Modern Physics* **59**, 1 (1987).
- [29] T. Schaetz, A. Friedenauer, H. Schmitz, L. Petersen, S. Kahra, *Journal of Modern Optics* **54**, 2317 (2007).
- [30] G. Clos, M. Enderlein, U. Warring, T. Schaetz, D. Leibfried, *Physical Review Letters* **112**, 113003 (2014).
- [31] M. Schreiber, *et al.*, *Science* **349**, 842 (2015).
- [32] G. Clos, H.-P. Breuer, *Physical Review A* **86**, 012115 (2012).
- [33] D. Porras, J. I. Cirac, *Physical Review Letters* **92**, 207901 (2004).
- [34] C. J. Myatt, *et al.*, *Nature* **403**, 269 (2000).
- [35] J. Smith, *et al.*, *arXiv:1508.07026* (2015).
-
- * govinda.clos@physik.uni-freiburg.de
- [1] J. v. Neumann, *Zeitschrift für Physik* **57**, 30 (1929).
- [2] Several different definitions of quantum integrability are commonly used in literature, for details see supplementary materials.
- [3] J. M. Deutsch, *Physical Review A* **43**, 2046 (1991).
- [4] M. Srednicki, *Physical Review E* **50**, 888 (1994).
- [5] M. Rigol, V. Dunjko, M. Olshanii, *Nature* **452**, 854 (2008).
- [6] M. Rigol, *Physical Review Letters* **103**, 100403 (2009).
- [7] L. F. Santos, M. Rigol, *Physical Review E* **81**, 036206 (2010).
- [8] W. Beugeling, R. Moessner, M. Haque, *Physical Review E* **89**, 042112 (2014).
- [9] H. Kim, T. N. Ikeda, D. A. Huse, *Physical Review E* **90**, 052105 (2014).
- [10] M. Srednicki, *Journal of Physics A: Mathematical and General* **32**, 1163 (1999).
- [11] S. Popescu, A. J. Short, A. Winter, *Nature Physics* **2**, 754 (2006).
- [12] P. Reimann, *Physical Review Letters* **101**, 190403 (2008).
- [13] N. Linden, S. Popescu, A. J. Short, A. Winter, *Physical Review E* **79**, 061103 (2009).
- [14] M. Cramer, J. Eisert, *New Journal of Physics* **12**, 055020 (2010).
- [15] A. J. Short, T. C. Farrelly, *New Journal of Physics* **14**, 013063 (2012).
- [16] J. Eisert, M. Friesdorf, C. Gogolin, *Nature Physics* **11**, 124 (2015).
- [17] M. A. Cazalilla, M. Rigol, *New Journal of Physics* **12**, 055006 (2010).
- [18] A. Polkovnikov, K. Sengupta, A. Silva, M. Vengalattore, *Reviews of Modern Physics* **83**, 863 (2011).
- [19] M. Gring, *et al.*, *Science* **337**, 1318 (2012).
- [20] S. Trotzky, *et al.*, *Nature Physics* **8**, 325 (2012).
- [21] T. Langen, *et al.*, *Science* **348**, 207 (2015).
- [22] D. Leibfried, R. Blatt, C. Monroe, D. Wineland, *Reviews of Modern Physics* **75**, 281 (2003).
- [23] C. Schneider, D. Porras, T. Schaetz, *Reports on Progress*

SUPPLEMENTARY MATERIAL

The trapped-ion Hamiltonian

Our system is fundamentally described by the total Hamiltonian [26]

$$H = \frac{\hbar\omega_z}{2}\sigma_z + \sum_{m=1}^N \hbar\omega_m a_m^\dagger a_m + \frac{\hbar\Omega_R}{2}(\sigma^+ e^{ik_L z} + \sigma^- e^{-ik_L z}), \quad (7)$$

in which the pseudo-spin is coupled to the motional reservoir through the recoil term $e^{ik_L z}$, where k_L is the effective wave vector of the coupling light field, and z the position of the pseudo-spin carrying ion. Note, that the last term in Eq. 7 induces both the term $(\hbar\Omega_R/2)\sigma_x$ and the spin-phonon coupling $(\hbar\Omega_R/2)(\sigma^+ C + \sigma^- C^\dagger)$ in Eq. 1 of the main text. The position z is efficiently expressed in terms of the motional modes

$$k_L z = \sum_{m=1}^N \eta_m (a_m^\dagger + a_m), \quad (8)$$

with corresponding Lamb-Dicke parameters

$$\eta_m = \mathcal{M}_m k_L \sqrt{\frac{\hbar}{2M\omega_m}}. \quad (9)$$

Here, M denotes the mass of the ion crystal, and \mathcal{M}_m is the wave-function amplitude of mode m at position z . Further, we express $\eta_m = \mathcal{M}_m \sqrt{\omega_1/\omega_m} \eta_1$, with η_1 corresponding to the center-of-mass ($m = 1$) mode. This form is convenient to quantify the strength of coupling induced by photon recoil in terms of the single parameter η_1 that is independent of N .

We recast Eq. 7 to the form of Eq. 1 and the operator C can be expanded as

$$C = i \sum_{m=1}^N \eta_m (a_m + a_m^\dagger) + O(\eta_m^2), \quad (10)$$

such that for values $\eta_m \ll 1$, we find linear/weak coupling that is commonly explored in trapped-ion experiments, while for $N \rightarrow \infty$ it sets the grounds for studying open quantum systems [28]. However, for values $\eta_m \gtrsim 1$, higher order phonon emission/absorption terms come into play. For our calculations, we take the full expression of C into account. Note, that the coupling strength can be effectively enhanced, as η_m scales with the Fock state $|n_m\rangle$: $\eta'_m \approx \eta_m \sqrt{1 + 2n_m}$. In our manuscript, we explicitly make use of the nonlinear/strong coupling and bring our system into a nonintegrable regime. The Hamiltonian (Eq. 7) is exactly solvable in the following cases: (i) $N = 1$ and $\omega_z = 0$, in which it corresponds to the quantum Rabi model [36], and (ii) $\Omega_R = 0$, in which

spins and bosons are not coupled at all. In any other region in parameter space, Eq. (7) can be considered a nonintegrable Hamiltonian by both of the applicable definitions of nonintegrability (i) it does not have an exact analytical solution, (ii) there is not a number of independent conserved observables that equals the number of degrees of freedom in the system [37]. To treat the quantum dynamics governed by Eq. 7 numerically, and accurately describe the thermalization process, we would need a quasi-exact method since aspects of thermalization, such as time scales and fluctuations critically depend on a complete evaluation of the set of frequencies involved in the dynamics. Standard approaches for the spin-boson model, such as path-integral methods or generalized master equations [38], rely on the assumption that the bosonic bath has a continuum spectrum of frequencies, and thus, they cannot be applied to our system with a discrete number of modes. The only reliable theoretical method to fully access the dynamics of thermalization in our system is, thus, a numerical Exact Diagonalization of the Hamiltonian.

Eigenstate Thermalization

We present the Eigenstate Thermalization Hypothesis (ETH) in more detail, and discuss the validity of the Inverse Participation Ratio (IPR) to quantify the ability of our system to thermalize [10, 13]. Assuming the set of energy eigenstates of the coupled system $\{|\psi_\beta\rangle\}$ and the pure state $|\phi_\alpha\rangle = \sum_\beta c_\beta(\alpha)|\psi_\beta\rangle$, the IPR is defined as

$$\text{IPR}(|\phi_\alpha\rangle) = \frac{1}{\sum_\beta |c_\beta(\alpha)|^4}. \quad (11)$$

We use the definition of thermalization as a process by which a system equilibrates to a thermal state such that mean values of local observables correspond to microcanonical averages [3, 4]. In particular, it needs two aspects:

- (a) Equivalence between time averages and microcanonical averages.
- (b) Equilibration around time averages, with fluctuations around the mean value that decrease as a function of the system size.

Recent work shows that large values of IPR lead to the fulfillment of condition (a), see for example [8]. Intuitively, we may expect that these lead to condition (b), as well. Indeed, an upper bound to fluctuations can be obtained by means of IPR [13]. However, we can show that for pure initial states, the ETH actually predicts not just an upper bound, but a scaling of fluctuations of local operators with $1/\sqrt{\text{IPR}}$. Below, we give a more detailed derivation of this scaling, which is implicitly shown in Ref. [10].

The ETH conjecture explains the mechanism behind thermalization of nonintegrable closed quantum systems by assuming that *thermalization occurs on the level of single eigenstates*. The meaning of this statement can be expressed as a condition of matrix elements of a local observable A in the eigenstate basis of the nonintegrable Hamiltonian [10],

$$\begin{aligned} A_{\beta_1, \beta_2} &= \langle \psi_{\beta_1} | A | \psi_{\beta_2} \rangle \\ &= \mathcal{A}(E) \delta_{\beta_1, \beta_2} + \frac{1}{\sqrt{D(E)}} f(E, \omega) R_{\beta_1, \beta_2}. \end{aligned} \quad (12)$$

Here, $E = (E_{\beta_1} + E_{\beta_2})/2$ and $\omega = (E_{\beta_1} - E_{\beta_2})/\hbar$, with the eigenenergies E_β of our coupled system, and $\mathcal{A}(E)$ is a smooth function of E that corresponds to the microcanonical average at energy E . The second term on the r.h.s. of Eq. 12 determines the nondiagonal matrix elements of A with a density of states $D(E) = \sum_\beta \delta(E - E_\beta)$. We note that $f(E, \omega)$ is a smooth real function of (E, ω) that is assumed to be normalized, $\int d\omega f(E, \omega)^2 \approx 1$. Additionally, it is centered around $\omega = 0$ and has a typical width $W(E)$ as a function of ω that determines the energy band of eigenstates yielding nonzero matrix elements. The set of complex numbers R_{β_1, β_2} is described by stochastic variables when averages are taken over the set of energy eigenstates

$$\sum_{\beta_1, \beta_2} \sum_{\beta'_1, \beta'_2} R_{\beta_1, \beta_2}^* R_{\beta'_1, \beta'_2} \propto \delta_{\beta_1, \beta'_1} \delta_{\beta_2, \beta'_2}, \quad (13)$$

where the proportionality factor depends on the operator A . In Reference [10], $D(E)$ is quantified by means of the entropy $e^{S(E)}$. Equation 12 is justified by assuming that the many-body eigenstates of a nonintegrable quantum system can be obtained by perturbing an initial integrable Hamiltonian, following the argument for the ETH in Ref. [3].

Building on that, we discuss the relation between IPR and fluctuations of A . We define time averages $\mu_\infty(A)$ and standard deviations $\delta_\infty(A)$, corresponding to the fluctuations of A , in the main text. Taking $|\phi_\alpha\rangle$ and nondegenerate energy gaps, we express fluctuations like [10]

$$\delta_\infty^2(A) = \sum_{\beta_1} \sum_{\beta_2 \neq \beta_1} |c_{\beta_1}(\alpha)|^2 |c_{\beta_2}(\alpha)|^2 |A_{\beta_1, \beta_2}|^2. \quad (14)$$

Using Equation 12, we get:

$$\begin{aligned} \delta_\infty^2(A) &= \sum_{\beta_1} \sum_{\beta_2 \neq \beta_1} |c_{\beta_1}(\alpha)|^2 |c_{\beta_2}(\alpha)|^2 \\ &\quad \times \frac{1}{D(E)} f(E, \omega)^2 |R_{\beta_1, \beta_2}|^2. \end{aligned} \quad (15)$$

Since $f(E, \omega)$ has width $W(E)$, the double sum in β_1, β_2 runs over energy eigenstates such that $E_{\beta_1} \approx E_{\beta_2} \pm W(E)$. There is a large number of those values, which

are assumed to be proportional to $D(E_{\beta_1})$. Thus, we can reduce the double sum in Eq. 15 to a single sum.

Further, we assume that $c_\beta(\alpha)$ are smooth functions of E_β , up to a random complex factor, such that $c_\beta(\alpha) \approx F(E_\beta, \alpha) C_{\beta, \alpha}$, where $C_{\beta, \alpha}$ can be considered as random numbers with the same statistical properties as R_{β_1, β_2} in Eq. 13, and $F(E_\beta, \alpha)$ is a smooth function of E_β determining the energy window of energy eigenstates taking part in $|\phi_\alpha\rangle$. Additionally, we assume that $D(E)$ and $F(E, \alpha)$ are constant within energy intervals on the order of the width of $f(E, \omega)$ and yield the following estimation for fluctuations

$$\begin{aligned} \delta_\infty^2(A) &\propto \int dE_{\beta_1} dE_{\beta_2} D(E_{\beta_1}) D(E_{\beta_2}) \\ &\quad \times F(E_{\beta_1}, \alpha)^2 F(E_{\beta_2}, \alpha)^2 \frac{1}{D(E)} f(E, \omega)^2 \\ &\approx \int dE D(E) F(E, \alpha)^4 \approx \sum_\beta |c_\beta(\alpha)|^4 \\ &= 1/\text{IPR}(|\phi_\alpha\rangle). \end{aligned} \quad (16)$$

We consider this a direct consequence of the set of conjectures and assumption underlying ETH.

In our experiment, the initial state is a product of a pure spin state and a mixed bosonic state. Thus, we need to find a method to average the IPR and get an appropriate measure of the effective dimension of an initial mixed state. In Reference [15] it is shown that, considering a mixed initial state $\rho(0) = \sum_\alpha w_\alpha |\phi_\alpha\rangle \langle \phi_\alpha|$, an upper bound to fluctuations around time-averaged states can be found from the definition $\text{IPR}^{-1}(\rho(0)) = \sum_\beta p_\beta^2$, with $p_\beta = \sum_\alpha w_\alpha |c_\beta(\alpha)|^2$. However, this approach has the disadvantage that the IPR takes large values for highly mixed initial states, even in the case of uncoupled systems, since then $c_\beta(\alpha) = \delta_{\beta, \alpha}$ and $\text{IPR}^{-1}(\rho(0)) = \sum_\alpha w_\alpha^2$. An alternative approach is to define an effective dimension by averaging over the IPRs of each state in the mixture, which directly leads to our definition in Eq. 3. This definition yields $D_{\text{eff}} = 1$ for uncoupled Hamiltonians and it takes large values only if interactions lead to a large number of Hamiltonian eigenstates participating in the thermalization process, thus, allowing us to detect regions where the system should be able to thermalize efficiently.

Numerical diagonalizations and their systematic uncertainties

We perform Exact Diagonalizations of Eq. 1 to calculate time evolutions $\langle \sigma_z(t) \rangle$ and microcanonical averages $\mu_{\text{micro}}(\sigma_z)$ with n_c (see Tab. I). Limited by computational power, calculations are done up to $\dim \mathcal{H} \approx 2^{13}$, e.g., corresponding to $N = 4$ and $n_c = 8$. For typical initial mode temperatures, this concurs with truncated initial-state populations $\text{tr} \bar{\rho}(0) \approx 0.85$. When numerical

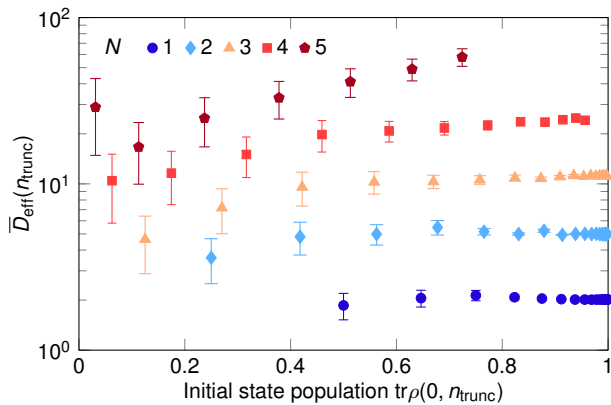


FIG. 5. Numerical study of D_{eff} as a function of truncated initial-state population for $N = 1 \dots 5$; explicitly, we plot our estimation $\overline{D}_{\text{eff}}(n_{\text{trunc}})$ (details see text). In the evaluation, the truncation $n_{\text{trunc}} = 1$ corresponds to lowest $\text{tr}\overline{\rho}(0)$, while n_{trunc} is increased in steps of one up to its maximum value n_c (limited by our computer memory; see Tab. I). The parameters are the same as in Fig. 1C: $\omega_1 = 2\pi \times 0.71$ MHz, $\eta_1 = 0.54$, $\bar{n}_{m=1\dots N} = 1$, $\Omega_R = 2\pi \times \{0.71, 0.97, 1.21, 1.46, 1.68\}$ MHz, $\omega_z = 0.8\omega_1$. For $N = 1 \dots 4$ and for $\text{tr}\overline{\rho}(0) > 0.5$, we find that $\overline{D}_{\text{eff}}(n_{\text{trunc}})$ agree within their attributed uncertainties (error bars) with numerically most accurate values $D_{\text{eff}}(n_c)$ as $\text{tr}\overline{\rho}(0, n_c) > 0.96$. This suggests that our procedure is reasonable even if about 0.5 of the initial-state population are neglected in the numerics.

results are less accurate (for $N = 5$), we omit displaying them in Figs. 2 and 3.

For calculations of D_{eff} , we use an approximation, i.e., we use a block-diagonalization procedure that exploits the band structure of our Hamiltonian matrix. We express Eq. 1 in the basis of eigenstates of the uncoupled system $|\phi_\alpha\rangle = |s\rangle|n_1\rangle_1 \dots |n_N\rangle_N$, with $s = \{\uparrow, \downarrow\}$, and $|n_m\rangle$ the Fock state with n phonons in the m th motional mode. The Hamiltonian takes the band matrix form,

$$H_{\alpha_1, \alpha_2} = \langle \phi_{\alpha_1} | H | \phi_{\alpha_2} \rangle = E_{\alpha_1}^{(0)} \delta_{\alpha_1, \alpha_2} + V_{\alpha_1, \alpha_2}, \quad (17)$$

with V_{α_1, α_2} the matrix of nondiagonal elements. We order the states according to their energy such that the diagonal entries $E_\alpha^{(0)}$ grow with index number

N		1,2		3		4		5	
Fig.	D_{eff}	n_c	$\text{tr}\overline{\rho}(0)$	n_c	$\text{tr}\overline{\rho}(0)$	n_c	$\text{tr}\overline{\rho}(0)$	n_c	$\text{tr}\overline{\rho}(0)$
1B	D_{eff}			10	0.94				
1C	D_{eff}	20	1.00	20	1.00	12	0.96	7	0.72
2	$\langle \sigma_z(t) \rangle$	20	1.00	11	0.97	6	0.72	(4)	(0.35)
3A	$\mu_{\text{micro}}(\sigma_z)$	20	1.00	16	0.99	8	0.86	5	0.46
3A	$\mu_{\text{exp}}(\sigma_z)$	20	1.00	9	0.93	5	0.62	(3)	(0.23)
3B	$\delta_{\text{exp}}(\sigma_z)$	20	1.00	9	0.93	5	0.62	(3)	(0.23)
4	D_{eff}	20	1.00	20	1.00	12	0.96	7	0.64

TABLE I. Cutoff in Fock space n_c and truncated initial-state population $\text{tr}\overline{\rho}(0)$ used in the numerical calculation for the different Figures.

$\alpha = 1 \dots \dim \overline{\mathcal{H}}$. The matrix V_{α_1, α_2} couples only those states that fulfill $|E_{\alpha_1}^{(0)} - E_{\alpha_2}^{(0)}| \lesssim |V_{\alpha_1, \alpha_2}|$. Further, we express the initial state $\rho(t=0) = \sum w_\gamma |\phi_\gamma\rangle \langle \phi_\gamma|$, calculate D_{eff} of each of the initial states $|\phi_\gamma\rangle$ by diagonalizing $H_{\alpha_1, \alpha_2}^{[\gamma]}$, and keep only quantum states α_1 and α_2 close to γ such that $(|\alpha_1 - \gamma|, |\alpha_2 - \gamma|) < N_{\text{states}}/2$, where N_{states} denotes the number of states kept to calculate the IPR of each of the states $|\phi_\gamma\rangle$. Thus, $H_{\alpha, \beta}^{[\gamma]}$ is projected onto a subspace of $N_{\text{states}} < \dim(\mathcal{H})$, that optimally contributes to D_{eff} of $|\phi_\gamma\rangle$. Finally, we diagonalize $H_{\alpha_1, \alpha_2}^{[\gamma]}$, calculate the contribution of $|\phi_\gamma\rangle$, and increase N_{states} by steps of 1000, until the resulting values of D_{eff} vary by less than 1% (5% for $N = 5$). For example, for $N = 4$, we use $n_c = 12$, corresponding to $\dim \overline{\mathcal{H}} \approx 2^{16}$, which converges using $N_{\text{states}} = 5000$. However, in the case of $N = 5$ and $n_c = 7$, we are (again) at the limit of our computational power, because we need $N_{\text{states}} = 20000$ for converged values of D_{eff} .

In the following, we describe our procedure to yield final values of D_{eff} including a measure of systematic uncertainties accounting for $\text{tr}\overline{\rho}(0) < 1$. We evaluate D_{eff} as a function of truncation $0 < n_{\text{trunc}} \leq n_c$ for all parameter settings presented in our manuscript (for a list of n_c see Tab. I). For each parameter setting, we calculate the truncated initial-state population $\text{tr}\overline{\rho}(0, n_{\text{trunc}})$, take $D_{\text{eff}}(n_{\text{trunc}})$ as a first bound $D_{\text{eff},1}$, linearly extrapolate from it a second bound $D_{\text{eff},2}$ with the slope extracted from $D_{\text{eff}}(n_{\text{trunc}} - 1)$, and plot $\overline{D}_{\text{eff}} \equiv (D_{\text{eff},1} + D_{\text{eff},2})/2$ as a function of $\text{tr}\overline{\rho}(0, n_{\text{trunc}})$. In Figure 5, we exemplary show this evaluation for $N = 1 \dots 5$ and parameters $\omega_1 = 2\pi \times 0.71$ MHz, $\eta_1 = 0.54$, $\bar{n}_{m=1\dots N} = 1$, $\Omega_R(N) = 2\pi \times \{0.71, 0.97, 1.21, 1.46, 1.68\}$ MHz, $\omega_z = 0.8\omega_1$. The error bars represent our attributed systematic uncertainties, given by $\pm |D_{\text{eff},1} - D_{\text{eff},2}|/4$. For $N = 1 \dots 4$ and all parameter settings, we find that, for $\text{tr}\overline{\rho}(0) > 0.5$, all extracted $\overline{D}_{\text{eff}}$ agree within their uncertainties with corresponding $D_{\text{eff}}(n_c)$, which, in turn, we consider most accurate, because for $N \leq 4$, it is ensured that $\text{tr}\overline{\rho}(0, n_c) > 0.96$. This suggests that our procedure yields reasonable values for D_{eff} even when up to 0.5 of the initial-state population is neglected in the numerical calculation, as it is the case for $N = 5$ and we use for final values $D_{\text{eff}} \equiv \overline{D}_{\text{eff}}(n_c)$, throughout the manuscript. Further, we apply a similar procedure, but based on Exact Diagonalization (no block-diagonalization), to provide final values of $\mu_{\text{micro}}(\sigma_z)$ including attributed systematic uncertainties.

Experimental setup

We employ a linear radio-frequency (rf) Paul trap with a drive frequency $\Omega_{\text{rf}} \approx 2\pi \times 56$ MHz to trap Mg^+ isotopes with secular frequencies of $\omega_{\text{rad},1,2} \approx 2\pi \times (4.0, 4.6)$ MHz (radial direction) and $\omega_1 \approx 2\pi \times 0.7$ MHz (axial

N	1	2	3	4	5
$\omega_1/(2\pi)$ (MHz)	0.724(2)	0.707(2)	0.707(2)	0.708(2)	0.709(2)
ω_N/ω_1	1.00(1)	1.73(1)	2.41(1)	3.05(1)	3.67(1)
$\omega_z/(2\pi)$ (MHz)	[0, 1.8]	[0, 2.2]	[0, 2.4]	[0, 2.5]	[0, 2.8]
$\Omega_R/(2\pi)$ (MHz)	0.73(1)	0.95(3)	1.28(3)	1.37(3)	1.58(5)
$\Delta_R/(2\pi)$ (GHz)	130(10)	110(10)	120(10)	110(10)	90(10)
n_{scat}	0.07(1)	0.07(1)	0.05(1)	0.05(1)	0.06(1)
\bar{n}_1	0.8(1)	0.3(1)	0.6(1)	0.7(2)	0.2(1)
\bar{n}_2		1.0(2)	1.1(2)	1.0(3)	1.0(2)
\bar{n}_3			0.9(2)	1.0(3)	1.1(2)
\bar{n}_4				1.0(4)	0.7(2)
\bar{n}_5					2.3(4)

TABLE II. Experimental parameters. Lowest (highest) frequency axial vibrational mode ω_1 (ω_N), transverse field ω_z varied within interval, Rabi frequency Ω_R , detuning Δ_R of the Raman beams from the $3S_{1/2}$ to $3P_{3/2}$ transition, calculated Raman scattering events n_{scat} during τ_{obs} , measured mode occupation number $\bar{n}_{m=1\dots N}$. Further, the detection duration is 40 μs for $N \leq 2$ and 80 μs for $N \geq 3$.

direction)[29]. Using a photoionization laser (wavelength $\lambda \approx 285$ nm), we isotope-selectively load $1 \times {}^{25}\text{Mg}^+$ and $(N-1) \times {}^{26}\text{Mg}^+$. Two electronic ground states of the hyperfine manifold of ${}^{25}\text{Mg}^+$ (nuclear spin $I_{25\text{Mg}} = 5/2$) constitute the pseudo-spin, $|\downarrow\rangle \equiv 3S_{1/2}|F=3, m_F=3\rangle$ and $|\uparrow\rangle \equiv 3S_{1/2}|F=2, m_F=2\rangle$, where F and m_F denote the total angular momentum quantum numbers of the valence electron. Note, that ${}^{26}\text{Mg}^+$ has no nuclear spin ($I_{26\text{Mg}} = 0$) and consequently, in our realization, it constitutes (only) to the motional mode structure.

To address transitions from $3S_{1/2}$ to either $3P_{1/2}$ or $3P_{3/2}$ in ${}^{25}\text{Mg}^+$ at wavelengths around 280 nm, we use dedicated all solid state laser systems [30, 39]: A laser beam with $\lambda_{\text{BD}} \approx 279.64$ nm (labelled BD) is tuned $\Gamma_{\text{nat}}/2$ below the $3S_{1/2}$ to $3P_{3/2}$ transition with natural line width $\Gamma_{P3/2} = 2\pi \times 41.8(4)$ MHz [40] and aligned with a magnetic quantization field $|\vec{B}| \simeq 0.58$ mT. The σ^+ -polarized light with intensity $I_{\text{BD}} \approx 0.5I_{\text{sat}}$ (saturation intensity $I_{\text{sat}} \simeq 2500$ W/m 2) is used for Doppler cooling to $\simeq 1$ mK and optical pumping to $|\downarrow\rangle$. This state provides efficient, state sensitive detection via closed cycling transition to $3P_{3/2}|4, 4\rangle$ to discriminate between the ground state manifolds. When BD is shifted near resonance (detuning $\leq 2\pi \times 4$ MHz), we observe a count rate of 100 ms^{-1} on average for all $F=3$ states and 2 ms^{-1} for the $F=2$ states. Two additional laser beams with $\lambda_{\text{RP}} \approx 280.35$ nm (labelled RP1 and RP2) are superimposed to BD and used for repumping electronic state population from $3S_{1/2}|F=3, m_F<3\rangle$ (RP1) and $3S_{1/2}|F=2\rangle$ (RP2) to $|\downarrow\rangle$ via $3P_{1/2}$ [with $\Gamma_{P1/2} = 2\pi \times 41.3(3)$ MHz [40]]. Further, two perpendicular laser beams at $\lambda_{\text{Raman}} \approx 279.61$ nm (labelled RR and BR) with a k -vector difference along the axial direction of the trap (ion-chain alignment) enable ground-state cooling of axial motional modes. This is achieved via sideband cooling with two-photon stimulated Raman transitions (TPSR) detuned by $\Delta_R = +2\pi \times 100(10)$

GHz from the $3S_{1/2}$ to $3P_{3/2}$ transition. In the regime of resolved sidebands, e.g., for $\omega_1 = 2\pi \times 1.90(1)$ MHz, $N \leq 3$, and $\Omega_R \leq 2\pi \times 0.5$ MHz, we routinely achieve occupation numbers $\bar{n}_{m=1\dots N} < 0.1$ by an iterative pulsed sideband cooling procedure. For $\omega_1 = 2\pi \times 0.71(1)$ MHz, we use $\Omega_R \approx 2\pi \times 0.25$ MHz and achieve $\bar{n}_{m=1\dots N} < 1$ for $N \leq 5$ by addressing several sideband transitions simultaneously. In Table II, we summarize relevant experimental parameters that are determined with dedicated calibration measurements, e.g., mode-temperature measurements [41].

The Hamiltonian (Eq. 1) is implemented via TPSR as well. In order to achieve strong coupling, i.e., Rabi frequencies up to $\Omega_R \approx 2\pi \times 1.6$ MHz, we use intensities $I_{\text{RR}} = 2.5(5) \times 10^3 I_{\text{sat}}$ and $I_{\text{BR}} \leq 0.8(1) \times 10^3 I_{\text{sat}}$. We employ two acousto-optical modulators to switch on and off beams (turn coupling on/off), to tune the relative frequency difference between RR and BR (varying ω_z), and to attenuate the intensity of BR (fine tune Ω_R).

At intensities I_{RR} and I_{BR} , the main contribution to decoherence in all our experiments, spontaneous Raman scattering rate of ${}^{25}\text{Mg}^+$ [42], is calculated to $\Gamma_R \leq 2\pi \times 1.2(1)$ kHz which corresponds to less than 0.07(1) scattering events in $\tau_{\text{obs}} = 13/\Omega_R$. This is in accordance with dedicated calibration measurements of the decoherence rate induced by RR and BR. We estimate the effect of the beams on the $(N-1) \times {}^{26}\text{Mg}^+$ for $N = 5$ where it is most significant due to smallest inter-ion distances in comparison to experiments with $N < 5$. Ion positions are calculated for $\omega_1 = 2\pi \times 0.71(1)$ MHz yielding $\vec{x} = \{0.0, 5.7, 11.0, 16.3, 22.0\}$ μm , with ${}^{25}\text{Mg}^+$ at $x = 0$. Assuming a relevant beam waist ($1/e^2$ radius of intensity) $w = 55(10)$ μm for RR and BR, the Raman scattering rates are estimated $\vec{\Gamma}_R \approx 2\pi \times \{1.2, 1.1, 1.1, 1.0, 0.9\}$ kHz resulting in an unwanted heating effect of less than 0.02 quanta (in τ_{obs}) distributed among N motional modes. In Figure 6, we compare typical experimental results for $\langle \sigma_z(t) \rangle$ to corresponding calculated unitary time evolutions with and without considering a decoherence rate γ . From this we infer that $\gamma\tau_R \lesssim 0.01$ such that decoherence contributes to a relative uncertainty of (in most cases much less than) 6% to our derived quantities during τ_{obs} . We neglect this effect throughout our manuscript since it is (much) smaller than the statistical uncertainties of the presented data. Hence, we consider our system completely isolated from external baths.

Optical pumping during detection

As the final step of our experimental sequences, we measure $\langle \sigma_z \rangle$. This is achieved by recording state-dependent fluorescence due to BD, shifted near resonance with an intensity $I_{\text{detect}} = 0.25I_{\text{sat}}$, for detection duration $T_{\text{detect}} = 40$ μs or 80 μs . During detection, $|\uparrow\rangle$ is off-resonantly pumped to $|\downarrow\rangle$ with a probability $P_{\downarrow}(t) = 1 - \exp(-\Gamma_{\text{leak}}t)$

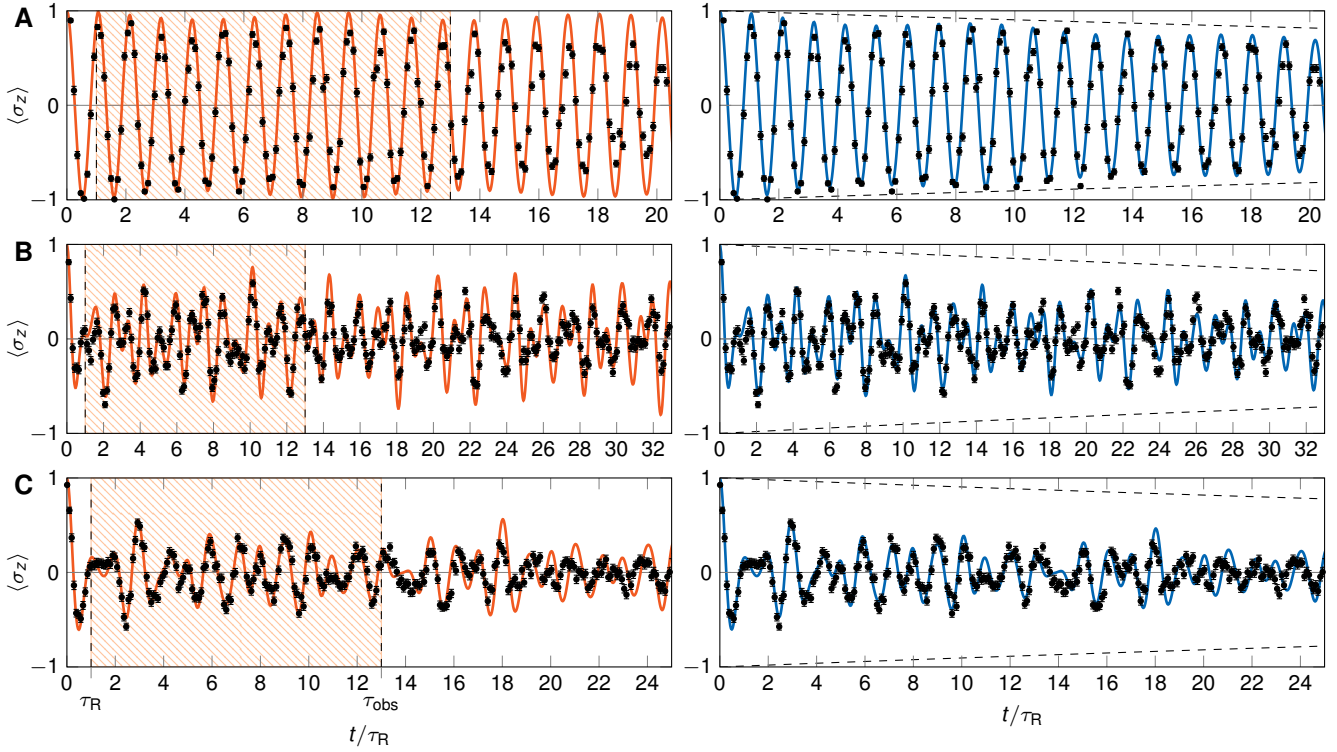


FIG. 6. Test for unitarity of the experimentally measured time evolutions. (left) Measured values with statistical uncertainties (black dots) and Exact Diagonalization of the unitary time evolution, i.e., with no decoherence (solid line). The shaded area emphasizes the time span that is considered to derive $\mu_{\text{exp}}(\sigma_z)$ and $\delta_{\text{exp}}(\sigma_z)$ (see Figs. 2 and 3), $1 \leq t/\tau_R \leq 13$. For $t/\tau_R \lesssim 15$ we find our experimental data in good agreement with Exact Diagonalizations. (right) The remaining discrepancy can be captured by implying a weak decoherence indicated by the dashed line $\langle \sigma'_z(t) \rangle = \langle \sigma_z(t) \rangle e^{-\gamma t}$, $\gamma\tau_R = 0.01$, which is in agreement with calculated spontaneous Raman scattering rates. Parameters for the experiments: (A) $N = 1$, $\{\omega_1, \Omega_R, \omega_z\} = 2\pi \times \{1.92(1), 0.685(5), 0.00(1)\}$ MHz, $\bar{n}_1 = 0.05(3)$ (B) $N = 1$, $\{\omega_1, \Omega_R, \omega_z\} = 2\pi \times \{0.73(1), 0.828(5), 0.00(1)\}$ MHz, $\bar{n}_1 = 0.6(1)$ (C) $N = 2$, $\{\omega_1, \Omega_R, \omega_z\} = 2\pi \times \{0.71(1), 0.940(5), 0.00(1)\}$ MHz, $\bar{n}_{\{1,2\}} = \{0.4(1), 0.6(1)\}$. This comparison justifies to treat our system as fully isolated within our experimental observation duration and, consequently, describe it by unitary time evolution.

where the estimated leak rate $\Gamma_{\text{leak}} \approx 2\pi \times 0.18$ kHz leads to $P_{\downarrow}(80 \mu\text{s}) = 0.09$. This unwanted effect yields a systematic altering of fluorescence photon-count histograms which we correct for, using dedicated calibration measurements, and recorded averaged fluorescence is adjusted by ≈ 0.03 .

Photon-count histograms

Measuring $\langle \sigma_z(t) \rangle$, each data point is derived by averaging over 500 realizations of the identical (fixed parameter settings) experiment consisting of (i) initialization (optical pumping and cooling), (ii) Hamiltonian interaction (laser pulses etc.), (iii) detection (fluorescence on PMT). To derive the probability P_{\downarrow} to be in the state $|\downarrow\rangle$ from the photon-count rate, we evaluate photon-count histograms. The statistics of the photon counts follows to good approximation a Poissonian distribution with expectation value λ where $\lambda_{\downarrow} \gg \lambda_{\uparrow} \approx 0$, where $\lambda_{\downarrow, \uparrow}$ are fixed for the analysis of each measured time evolution. Considering a weighted combination of these two Poissonian distribu-

tions, we extract $P_{\downarrow, \uparrow}$ and, subsequently, $\langle \sigma_z \rangle = 2P_{\downarrow} - 1$. The statistical uncertainty of $\langle \sigma_z \rangle$ is determined by the covariance of the maximum-likelihood fit of the weight [43].

Spatial ordering of the Coulomb crystal

To ensure overlap of $^{25}\text{Mg}^+$ (the pseudo-spin carrying ion) with all laser beams as well as constant detection efficiency, we initialize the ion-chain order prior to each measurement (every 500 experiments). Following Ref. [44], we utilize (a) the mass dependency of the harmonic pseudo-potential (b) a radial bias field and (c) the light pressure from BD. In preparation of measurements, we align all lasers onto $^{25}\text{Mg}^+$ and center an aperture in front of the PMT. In this way, we can detect experiments, in which the ion-chain order is disturbed, by a systematic change in photon-count histograms. We postselect experiments where the desired ion-order is achieved which is true in $\{97.1(3), 82(2), 81(1), 79(2)\}$ % of all our experiments for $N = 2 \dots 5$.

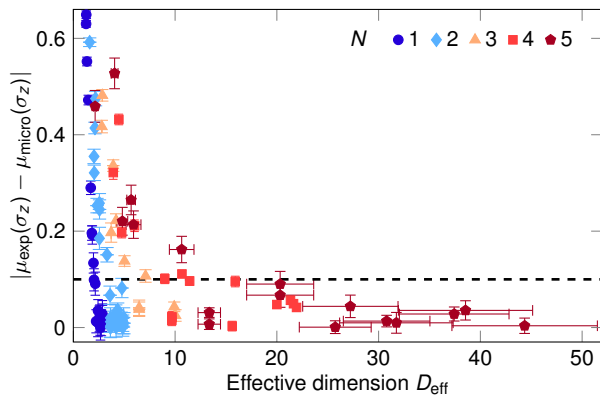


FIG. 7. Comparison of experimental results to microcanonical averages. Deviation from $\mu_{\text{micro}}(\sigma_z)$ (with statistical uncertainties) as a function of D_{eff} (with systematic uncertainties) for $N = 1 \dots 5$. We observe $1 < D_{\text{eff}} < 50$, while the spreads of $D_{\text{eff}}(N)$ overlap and grow with increasing N . At fixed N , $\mu_{\text{exp}}(\sigma_z)$ approaches $\mu_{\text{micro}}(\sigma_z)$ with increasing D_{eff} and the points with a deviation ≤ 0.1 (dashed line) are used for evaluation in Fig. 4.

Applicability of microcanonical averages

In Figure 3A, we display time averages $\mu_{\text{exp}}(\sigma_z)$ as a function of transverse field ω_z for $N = 1 \dots 5$ and compare them with the microcanonical ensemble averages $\mu_{\text{micro}}(\sigma_z)$. We correlate the deviation $|\mu_{\text{exp}}(\sigma_z) - \mu_{\text{micro}}(\sigma_z)|$ with the corresponding effective dimension D_{eff} for each data point, see Fig. 7. For this sampling of ω_z , we find D_{eff} lying between 1 and 50, e.g., for $N = 2$ it can be tuned from 2 to 5, while for $N = 5$ the spread is 2 to 50. This implies that we can explicitly compare

experiments which have equal D_{eff} despite distinct values of N . Further, Fig. 7, and accompanying numerical calculations, suggest that we can continuously scale D_{eff} by increasing N and, particularly, tuning ω_z . Our definition of D_{eff} measures the ability of our system to thermalize, in the sense that $\mu_{\text{exp}}(\sigma_z)$ approach $\mu_{\text{micro}}(\sigma_z)$ as D_{eff} increases. Based on this, we select the data points for which we study the correlations between fluctuations and effective dimension in Fig. 4: The dashed line in Fig. 7 indicates a deviation of 0.1, all measurements closer to $\mu_{\text{micro}}(\sigma_z)$ are taken into account in Fig. 4.

* govinda.clos@physik.uni-freiburg.de

- [36] D. Braak, *Physical Review Letters* **107**, 100401 (2011).
- [37] J.-S. Caux, J. Mossel, *Journal of Statistical Mechanics: Theory and Experiment* **2011**, P02023 (2011).
- [38] U. Weiss, *Quantum Dissipative Systems* (World Scientific, 1999).
- [39] A. Friedenauer, *et al.*, *Applied Physics B* **84**, 371 (2006).
- [40] W. Ansbacher, Y. Li, E. Pinnington, *Physics Letters A* **139**, 165 (1989).
- [41] D. J. Wineland, *et al.*, *Journal of Research of the National Institute of Standards and Technology* **103**, 259 (1998).
- [42] R. Ozeri, *et al.*, *Physical Review A* **75**, 042329 (2007).
- [43] C. E. Langer, High Fidelity Quantum Information Processing with Trapped Ions, Ph.D. thesis, Department of Physics, University of Colorado, Boulder (2006).
- [44] D. Hume, Two-Species Ion Arrays for Quantum Logic Spectroscopy and Entanglement Generation, Ph.D. thesis, Department of Physics, University of Colorado, Boulder (2010).